

# Cryo-electron tomography reconstructs polymer in liquid film for fab-compatible lithography

Received: 16 April 2025

Accepted: 26 August 2025

Published online: 30 September 2025

Liming Zheng  <sup>1,8</sup>, Yijie Xia <sup>1,8</sup>, Xia Jia <sup>2,8</sup>, Mingyi Gao <sup>3</sup>, Nan Liu  <sup>4</sup> , Jiling Song  <sup>2</sup>, XiaoPeng Li <sup>2</sup>, Xiaole Zhao <sup>1</sup>, Xin Gao  <sup>1</sup>, Wen Zhou  <sup>1</sup>, Wenbing Kang  <sup>5</sup>, Lijiang Yang <sup>1</sup>, Qianqian Wang <sup>5</sup>, Yiqin Gao  <sup>1,6,7</sup> , Hong-Wei Wang  <sup>2</sup>  & Hailin Peng  <sup>1</sup> 

 Check for updates

Liquid film is ubiquitous in nature and serves as the critical medium for the dissolution of photoresist to create nanoscale circuit patterns in lithography, which is a core task since the birth of semiconductor industry. However, despite decades of research, the microscopic behaviors of photoresist in liquid film and at interfaces remain elusive, leading to industrial effort for pattern defect control largely a trial-and-error process. Here, we unravel the nanostructures and dynamics of photoresist polymers in liquid film and at gas-liquid interface using a cryo-electron tomography (cryo-ET) methodology. The native-state three-dimensional structures of photoresist polymers are reconstructed by cryo-ET at significantly improved resolution compared to conventional methods. Cryo-ET reconstructions resolve the spatial distributions of photoresist polymers across gas-liquid interface into bulk solution, revealing the cohesional entanglements between polymer chains. By inhibiting the polymer entanglements and leveraging photoresist's adsorption at gas-liquid interface, the contaminations across 12 inch wafers have been eliminated under industrial conditions, yielding a > 99% improvement in minimizing the pattern defects for fab-compatible lithography.

Liquid films are widely involved in various physical, chemical and biological processes, such as ice melting, liquid freezing, aqueous reaction, and tear film of the eye<sup>1–4</sup>. Liquid films also contribute to advancements in human civilization, exemplified by 193 nm immersion lithography<sup>5,6</sup>, which is widely used in modern semiconductor fabs to manufacture sub-7 nm node electronics<sup>7</sup>. In this technology, introducing a water film between lens element and photoresist to replace the

air gap can generate a shorter wavelength  $\lambda_{\text{water}}$ , because  $\lambda_{\text{water}} = \lambda_{\text{air}}/1.33$ . The shorter wavelength enables a smaller resolution limit, thereby establishing a prerequisite for continuous downscaling of integrated circuits. In the era of extreme ultraviolet (EUV) lithography<sup>8,9</sup>, liquid film continues to play a critical role in the formation of circuit patterns. During photoresist development—a fundamental step in lithography—the exposed regions of photoresist are selectively dissolved in the

<sup>1</sup>Beijing National Laboratory for Molecular Sciences, College of Chemistry and Molecular Engineering, Peking University, Beijing 100871, China. <sup>2</sup>Ministry of Education Key Laboratory of Protein Sciences, Beijing Frontier Research Center for Biological Structures, Tsinghua-Peking Joint Center for Life Sciences, School of Life Sciences, Tsinghua University, Beijing 100084, China. <sup>3</sup>Hangzhou STS Semiconductor Technology Co, Hangzhou 311107 Zhejiang, China.

<sup>4</sup>School of Biological Sciences, The University of Hong Kong, Hong Kong 999077, China. <sup>5</sup>National Engineering Research Center for Colloidal Materials, School of Chemistry and Chemical Engineering, Shandong University, Jinan 250100 Shandong, China. <sup>6</sup>Changping Laboratory, Beijing 102200, China.

<sup>7</sup>Biomedical Pioneering Innovation Center (BIOPIC), Peking University, Beijing 100871, China. <sup>8</sup>These authors contributed equally: Liming Zheng, Yijie Xia, Xia Jia.  e-mail: [nanliu@hku.hk](mailto:nanliu@hku.hk); [gaoyq@pku.edu.cn](mailto:gaoyq@pku.edu.cn); [hongweiwang@tsinghua.edu.cn](mailto:hongweiwang@tsinghua.edu.cn); [hlpeng@pku.edu.cn](mailto:hlpeng@pku.edu.cn)

liquid films of developer solution<sup>10</sup>. This liquid-mediated process precisely transfers the EUV-exposed patterns into three-dimensional nanostructures with sub-10 nm resolution. As the feature size of pattern approaches the contour length of photoresist polymers, the adsorption and entanglement behaviors of photoresist molecules within liquid films emerge as essential factors governing defect formation on patterned surfaces (Fig. S1), ultimately determining the stability and production yield of semiconductor devices<sup>10–12</sup>. However, these microscopic behaviors of photoresist polymers in liquid films and at aqueous interfaces are still poorly understood, impeding the next-generation materials-technology co-optimization for high volume manufacturing.

The main bottleneck in deciphering the underlying processes in the liquid film during photoresist development stems from the absence of a suitable high-resolution imaging technique. Scanning electron microscopy (SEM) has been widely used in semiconductor industry for viewing the final structures of photoresist patterns, but it is not capable of imaging photoresist in solution. Atomic force microscopy (AFM)<sup>13,14</sup> and quartz crystal microbalance (QCM)<sup>15</sup> can be introduced to study the photoresist dissolution, yet the available information is still too limited for understanding the complex physicochemical phenomena occurring at microscopic interfaces with high resolution<sup>16</sup>. Currently, the use of indirect-imaging and relatively low-resolution characterization techniques constrains our insight into photoresist behaviors in liquid films and at microscopic interfaces, leading to the industrial optimization of photoresist development largely a trial-and-error process.

To address these challenges, we develop a cryo-electron tomography (cryo-ET) to reveal the photoresist behaviors in liquid films. Compared with conventional methods, the cryo-ET analysis offers several noticeable advantages: (1) native structures of polymer-based photoresist in liquid films are maintained during imaging, (2) three-

dimensional structures and interfacial distributions of photoresist polymers in liquid films are reconstructed at high resolution, (3) polymer entanglements of photoresist molecules can also be resolved. With our insights to photoresist behaviors revealed by cryo-ET in the lab, an industrial-scale photoresist development with eliminated defect for high-resolution lithography has been achieved in the fab.

## Results

### Process design for reconstructing photoresist polymers in liquid films

In modern semiconductor industry, chemically amplified resist is the workhorse photoresist used in 193 nm immersion lithography and EUV lithography for high volume manufacturing<sup>17–19</sup>. Therefore, we chose a widely-used poly(methacrylate)-based chemically amplified resist as our model photoresist. To prepare the specimen (photoresist dissolved in liquid film) for cryo-ET imaging, lithography and plunge freezing techniques have been integrated. As shown in Fig. 1a, the photoresist is spin-coated on a semiconductor wafer, and ultraviolet light transfers patterning information from a mask onto the photoresist film. The exposed areas of photoresist experience a significant change in solubility, following which a developer solution is sprayed—forming a thin liquid film on the photoresist surface. After the exposed photoresist is dissolved into the liquid film, the solution containing photoresist polymers is pipetted onto a TEM grid from the resist substrate. The grid subsequently undergoes a blotting process and plunge freezing to cryogenic temperatures (77 K), resulting in a thin vitreous ice layer with embedded photoresist polymers (Fig. 1a, Fig. S2). The plunge freezing technique, adapted from cryo-specimen preparation protocols used in structural biology (Fig. S2), achieves an ultrafast cooling rate ( $>10^4$  K/s)<sup>20,21</sup> that enables the trapping of photoresist polymers in their native solution-phase conformations.

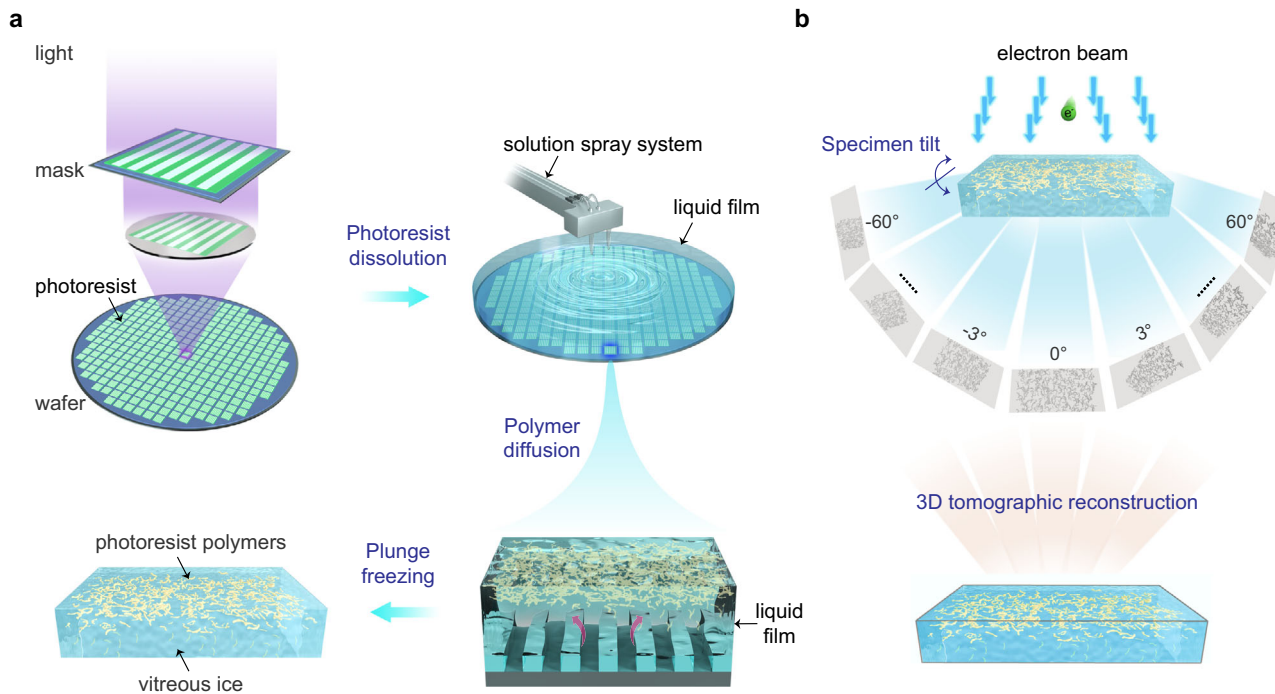


**Fig. 1 | Design of cryo-ET reconstruction for photoresist polymers in a liquid film.** **a** Schematic of preparing the photoresist specimen in a vitrified liquid film. Ultraviolet light transfers pre-designed pattern onto the polymer-based photoresist on a wafer. The exposed photoresist is subsequently dissolved in a liquid film of developer, which further undergoes plunge freezing to immobilize the photoresist polymers in the vitreous ice for preserving polymers' native

hydrated state. **b** Schematic showing cryo-ET reconstruction of photoresist polymers in the vitreous ice. A series of images captured from tilted angles ranging from  $-60^\circ$  to  $+60^\circ$  with  $3^\circ$  increments are collected to obtain multidirectional projections of the photoresist polymers, which are processed for 3D reconstructions of photoresist polymers in the vitreous ice.

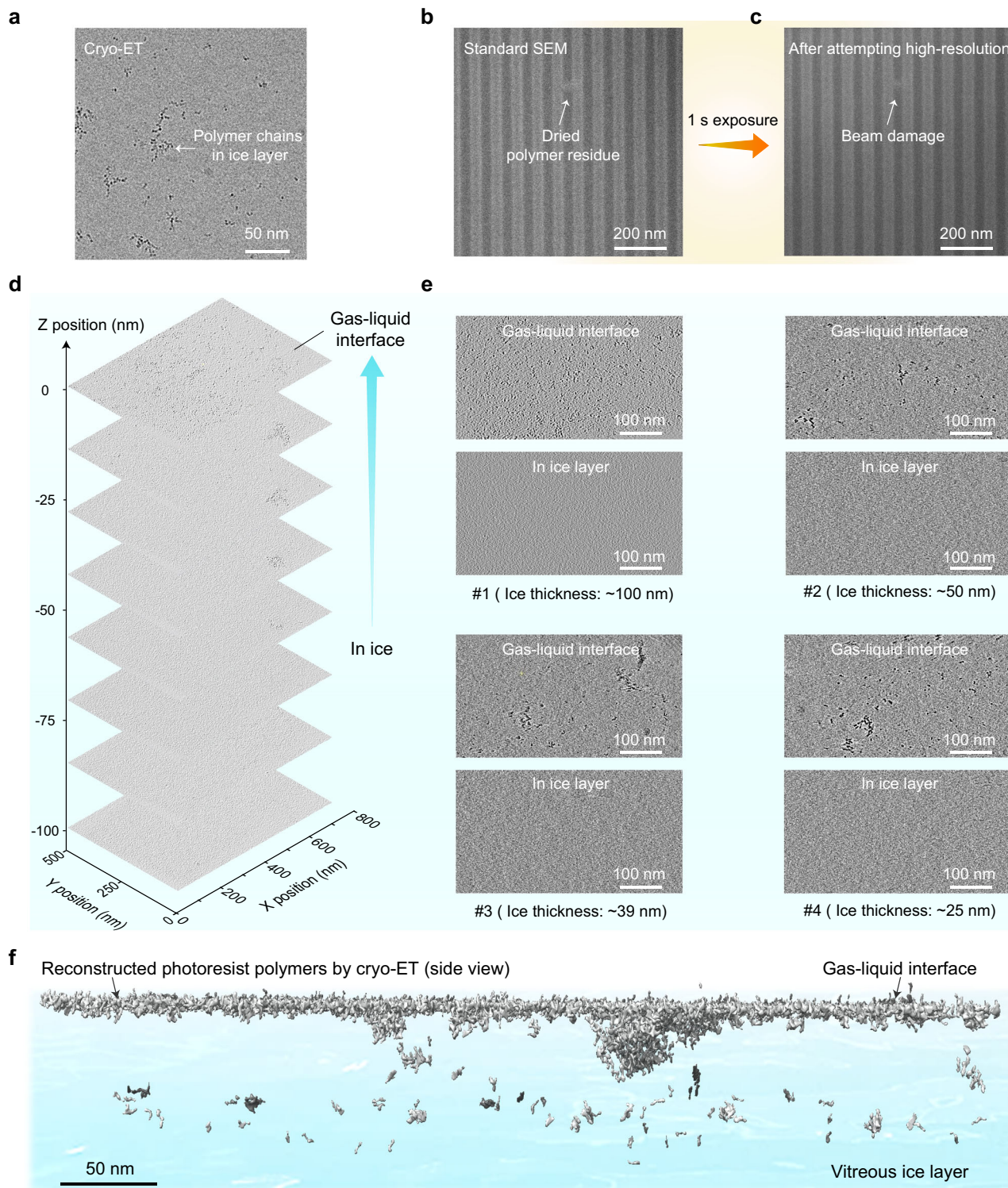


**Fig. 2 | Native structures and interfacial distributions of photoresist polymers within liquid films.** **a** A projection image from cryo-ET showing the photoresist polymers embedded in a rapidly vitrified liquid film with preserved native nanoscale structure. **b** Standard SEM image of a dried photoresist residue adsorbed on the pattern surface. **c** Standard SEM image of photoresist residue from (b) after exposure to a low beam current of  $\sim 0.05$  nA for 1 s. The dimensions of the photoresist residue exhibit significant shrinkage under this exposure. **d** Cryo-electron

tomographic slices reveal heterogeneous photoresist polymer distribution from gas-liquid interface to bulk solution within the vitrified liquid film of  $\sim 100$  nm. **e** Representative cryo-ET slices resolving the polymer distributions within vitrified liquid films of varying thicknesses. **f** Side view of reconstructed tomogram, highlighting high-contrast densities that correspond to photoresist polymers. Most photoresist polymers tend to adsorb at the gas-liquid interface.

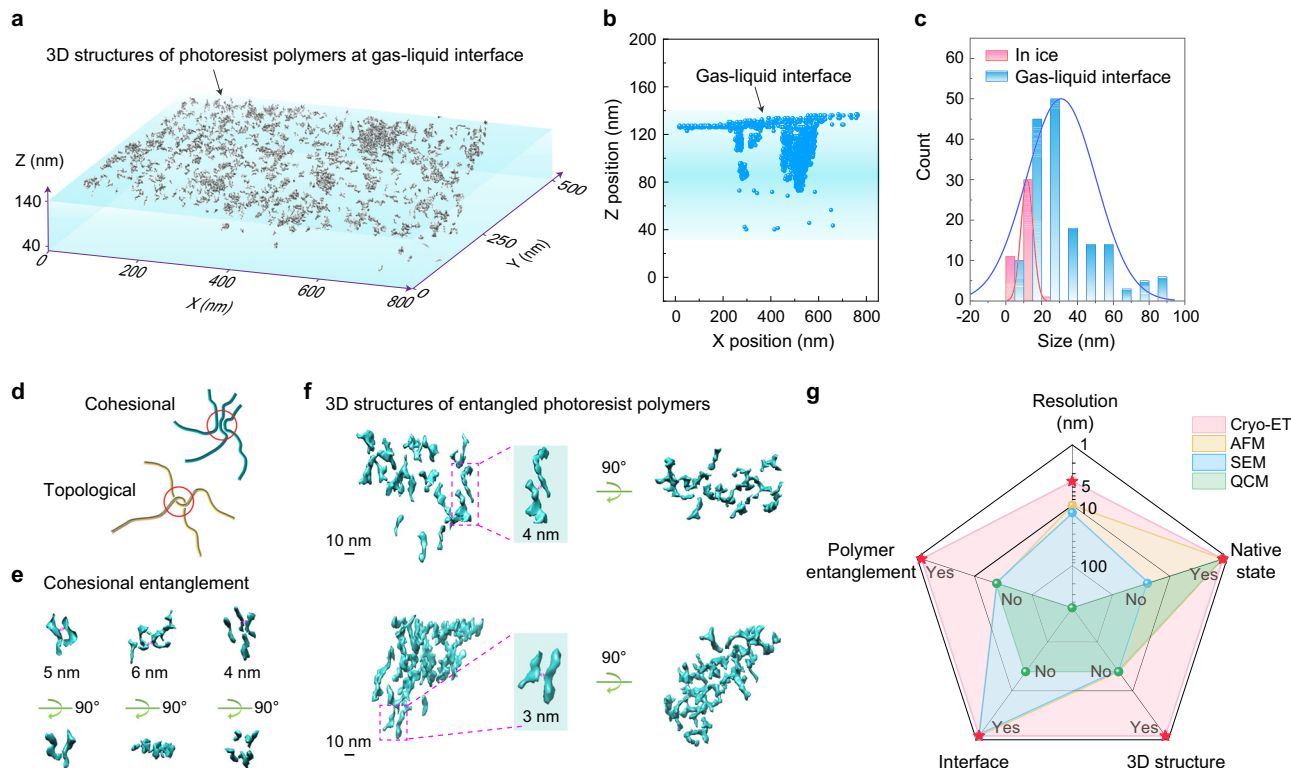


**Fig. 3 | Structural reconstructions and polymer entanglements of photoresist within liquid films.** **a** 3D tomogram reconstruction of photoresist polymers in the vitrified liquid film. **b** Spatial locations of photoresist densities in **(a)**. The blue spots represent the photoresist densities. **c** Size distributions of photoresist polymers at the gas-liquid interface (blue) and in the ice layer (red). **d** Schematic of two types of polymer entanglements: localized parallel segments in cohesional entanglement (top) versus physically interlocked loops in topological entanglement (bottom).

**e** 3D reconstructions of parallel chain segments indicating the cohesional entanglement between photoresist molecules. **f** Representative 3D reconstructions of entangled polymers from gas-liquid interface. The sub-5 nm spacings between polymer chains can be resolved. **g** A comparative radar plot benchmarking cryo-ET against conventional imaging methods<sup>12–15</sup> across five metrics: resolution, native-state preservation, 3D structural reconstruction, interface distribution analysis, and polymer entanglement characterization.

Moreover, under cryogenic conditions, the electron-beam-induced damage is significantly suppressed<sup>22–24</sup>, which contributes to preserving the pristine structural conformations of photoresist polymers during cryo-ET imaging. By leveraging this advantage, a tilt series of images (angular range:  $-60^\circ$  ~  $+60^\circ$ ) are acquired to capture the multidirectional projections of polymer chains (Fig. 1b). These projections enable the tomographic reconstructions of three-dimensional (3D) structures, interfacial distributions and polymer entanglements of photoresist polymers within liquid films (Fig. 1b & S2).

**Cryo-ET visualization of photoresist polymers and interfaces**  
 Figure 2a shows a representative cryo-ET slice of photoresist polymers embedded in vitreous ice. The polymer chains exhibit high contrast against the background, enabling clear visualization of their random coil conformations (Fig. 2a). These random coil structures were consistently observed across multiple samples (Fig. S3), closely resembling the polymer conformations reported in dilute solutions<sup>25</sup>. This agreement suggests that rapid vitrification preserves the photoresist polymers in their native hydrated state. In contrast, conventional SEM method was limited to imaging dried polymer residues on the patterned surface (Fig. 2b), resulting in relatively lower resolution and compromised structural information. Furthermore, the photoresist residue was sensitive to the electron beam irradiation, sustaining significant damage after just 1 s of exposure to a low beam current of  $\sim 0.05$  nA in the SEM (Fig. 2c). Besides beam-induced damage, the electron beam irradiation from SEM caused charging effects on the polymer surface, which distorted morphological features and introduced resolution artifacts (Fig. S4). This discrepancy was clearly demonstrated when comparing SEM data

with charge-sensitive AFM measurements of the same irradiated area (Fig. S4).

Beyond preserving the native state of photoresist polymers, cryo-ET enables nanoscale mapping of their spatial distribution within liquid films. Figure 2d presents the tomographic slices through z axis, revealing the distribution of photoresist polymers across gas-liquid interface into bulk solution. These slices showed that most photoresist polymers tended to adsorb at the gas-liquid interface, while few polymers located in the bulk solution (Fig. 2d). Similar preferential interfacial adsorption was also observed in both 248 nm chemically amplified resist and 365 nm i-line photoresist systems (Fig. S5). This phenomenon is very different from the conventional thought in industry that dissolved photoresist polymers mainly disperse in the bulk solution<sup>26,27</sup>. To verify this, we performed multiple independent experiments and systematically investigated the impact of liquid film thickness on the polymer distribution at interfaces. As shown in Fig. 2e, photoresist polymers predominantly adsorbed at gas-liquid interfaces across all samples, with liquid film thicknesses ranging from 25 nm ~ 100 nm (Fig. S6). Besides, we conducted cryo-ET to examine the developer solution as a blank control. As a result, no polymers were detected at the gas-liquid interface or in bulk solution (Fig. S7). When the photoresist polymers were reintroduced into the blank developer solution, these polymers reappeared at the gas-liquid interface (Fig. S7). X-ray photoelectron spectroscopy analysis further identified the presence of poly(methacrylate) in the photoresist polymers collected from gas-liquid interface (Fig. S8, Methods). Using the cryo-ET tomogram in Fig. 2d, we reconstructed the spatial distribution of photoresist polymers within the liquid film. The cryo-ET side-view reconstruction directly demonstrated the preferential adsorption of

photoresist polymers at the gas-liquid interface (Fig. 2f), as evidenced by a drastic decay in polymer density from the interface towards the bulk liquid phase.

### 3D structures and polymer entanglements of photoresist in liquid films

Figure 3a reveals the 3D tomogram map of photoresist polymers in vitreous ice at nanometer resolution, which provides crucial insights into polymer 3D structures and chain entanglements at the gas-liquid interface and in the liquid phase, respectively. From this 3D tomogram, we can determine the spatial positions of each photoresist polymer in the vitrified liquid film (Fig. 3b). Around 80% photoresist polymers adsorb at gas-liquid interface, while only ~20% photoresist molecules remain in the liquid. Meanwhile, the structural morphologies of photoresist at gas-liquid interface show significant differences from those in the liquid phase. Most photoresist polymers in liquid phase remain dispersed and disengaged (Fig. S9), a behavior consistent with polymer chains in sufficiently dilute solutions<sup>28</sup>. The average length of these liquid-phase polymers is ~12 nm (Fig. 3c), aligning with the reported chain length of poly(methacrylate)-based photoresist<sup>10</sup>. In contrast, photoresist polymers tend to entangle forming large particles at the gas-liquid interface (Fig. 3a, Fig. S9). The statistic results show that the average size of photoresist polymers at gas-liquid interface is around 30 nm, and the photoresist particles over 40 nm account for ~20% (Fig. 3c). Such large-sized particles may pose a risk of defect formation due to their adsorption on the pattern surface during photoresist development (Fig. S1).

Regarding the structural determination of polymer entanglement, cryo-ET provides a powerful tool to resolve the topological features of polymer chains—a challenge previously hindered by the lack of direct visualization methods<sup>29</sup>. Entanglement in polymers is generally defined as two types: cohesional entanglement and topological entanglement (Fig. 3d). The cohesional entanglement features local aligned chain segments with weak interaction, while the topological entanglement is characterized by interlocked chain loops and requires at least 130 - 350 monomer units<sup>30</sup>. In our cryo-ET reconstruction, localized parallel chain segments, indicative of cohesional polymer entanglement, were frequently observed (Fig. 3e). The inter-segment spacing of these entangled regions was on the order of several nanometers (Fig. 3e), matching the characteristic scale of polymer entanglement. Additionally, the large-sized particles at the gas-liquid interface actually exhibited loosely packed 3D architectures (Fig. 3f), with sub-5 nm inter-chain distances suggesting weak intermolecular interactions. These findings demonstrate that photoresist polymers form entanglements primarily via cohesional interactions rather than topological constraints—a conclusion further validated by their low molecular weight (<100 monomer units) (Fig. S10).

Based on the results and analyses above, compared to conventional established characterization methods<sup>12-15</sup>, the cryo-ET methodology demonstrates significant advances in visualizing the polymers within liquid films across five metrics: native-state preservation, interfacial distribution analysis, 3D structural reconstruction, high resolution (sub-5 nm), and polymer entanglement visualization (Fig. 3g).

### Simulation of photoresist dynamics in liquid films

In addition to the 3D cryo-ET reconstructions, we conducted molecular dynamics (MD) simulations to elucidate the diffusion and entanglement behavior of photoresist polymers in liquid films. Poly(methacrylate) and poly(methacrylic acid) were employed as model polymers in MD simulations (Fig. 4a), based on their roles as the key pre-exposure and post-exposure components in ultraviolet-triggered chemically amplified resists<sup>31</sup>. When a poly(methacrylic acid) molecule is placed in a water slab, it diffused to the gas-liquid interface spontaneously in the simulation (Fig. 4b). The z-direction spatial distribution further demonstrates the adsorption of poly(methacrylic acid) at

the gas-liquid interface (Fig. 4c). Meanwhile, the potential of mean force was calculated from the z-direction distribution function of poly(methacrylic acid) (Fig. 4d, Methods). The significant decrease in the potential of mean force revealed that the distribution of photoresist polymers at the gas-liquid interface is thermodynamically favorable (Fig. 4d).

To investigate the entanglement between photoresist polymers, we studied the dynamics of a solution containing two initially separated poly(methacrylic acid) molecules (Fig. 4e). In the simulation, the two molecules quickly approached each other and formed cohesional entanglement between several monomer units of the two polymer chains (Fig. 4g, state 2). As the simulation progresses, the polymer chains diffused to the gas-liquid interface, along with increased entanglements between them (Fig. 4g, from state 3 to state 5). Each entangled state was accompanied by a slight reduction in energy compared to the previous state (Fig. 4g), indicating the cohesional entanglement of polymer was energy-driven, in particular through van der Waals interactions (Fig. 4f, g). The entangling interactions are thus relatively weak, making both the entanglement and disentanglement processes highly dynamic (Fig. S11). We further studied the dynamics of poly(methacrylate) molecules in liquid films using MD simulations. Similarly, the poly(methacrylate) molecules tended to diffuse to the gas-liquid interface (Fig. S12), and formed cohesional entanglement through the hydrophobic interactions between the ester groups of poly(methacrylate) molecules (Fig. S13). These simulation results are in good agreement with experimental cryo-ET reconstructions and provide insights into the understanding of photoresist dynamics in liquid films at atomic scale.

### Defect control for fab-compatible photoresist development

With uncovered entanglement and adsorption behaviors of photoresist in liquid films, we further validate their potential in reducing the pattern defect of industrial-scale photoresist development, which is a persistent challenge in high-resolution lithography<sup>11</sup>. Figure 5a shows a 12 inch wafer patterned with chemically amplified resist, where critical dimensions of 38-40 nm can be achieved (Fig. 5b). Notably, these sub-40 nm dimensions are approaching the resolution limit of 193 nm immersion lithography (38 nm, Fig. S14). Our cryo-ET reconstruction reveals that large-sized photoresist particles over 40 nm constitute ~20% (Fig. 3c). Once these entangled particles adsorb onto the pattern surface, pattern defects are likely to form. This phenomenon actually often occurs under the working conditions of industrial photoresist development. The commonly-used chemically amplified resist is designed to be very hydrophobic<sup>31</sup> with a high water contact angle of ~85° (Fig. 5c). The poor wettability induced de-wetting can easily cause the redeposition of entangled polymer residues onto the pattern surface, directly driving defect formation (Fig. 5d, Fig. S15). Figure 5e exhibits a representative pattern defect with a polymer residue bridging the trenches. Based on the defect mapping, the defect count can reach up to 6617 across a 12 inch wafer (Fig. 5e), a level unacceptable in high-volume manufacturing.

In light of this, inhibiting the polymer entanglement during the photoresist development may provide a key to alleviating the defect formation on the pattern surface. As revealed by our cryo-ET reconstructions and MD simulations, the entangled photoresist residues are mainly formed by weak cohesional interactions, which are simple to unravel and strongly temperature dependent<sup>29</sup>. When increasing the post exposure bake (PEB) temperature during lithography process, we found that the polymer entanglement could be efficiently suppressed (Fig. 5g). With a treatment of a relatively low PEB temperature (95 °C), the photoresist particles at gas-liquid interface exhibited an entangled morphology with a lateral size of 40 - 80 nanometers (Fig. 5g, left panel). In contrast, the photoresist polymers tended to be disentangled and separated with reduced contour length, when the PEB

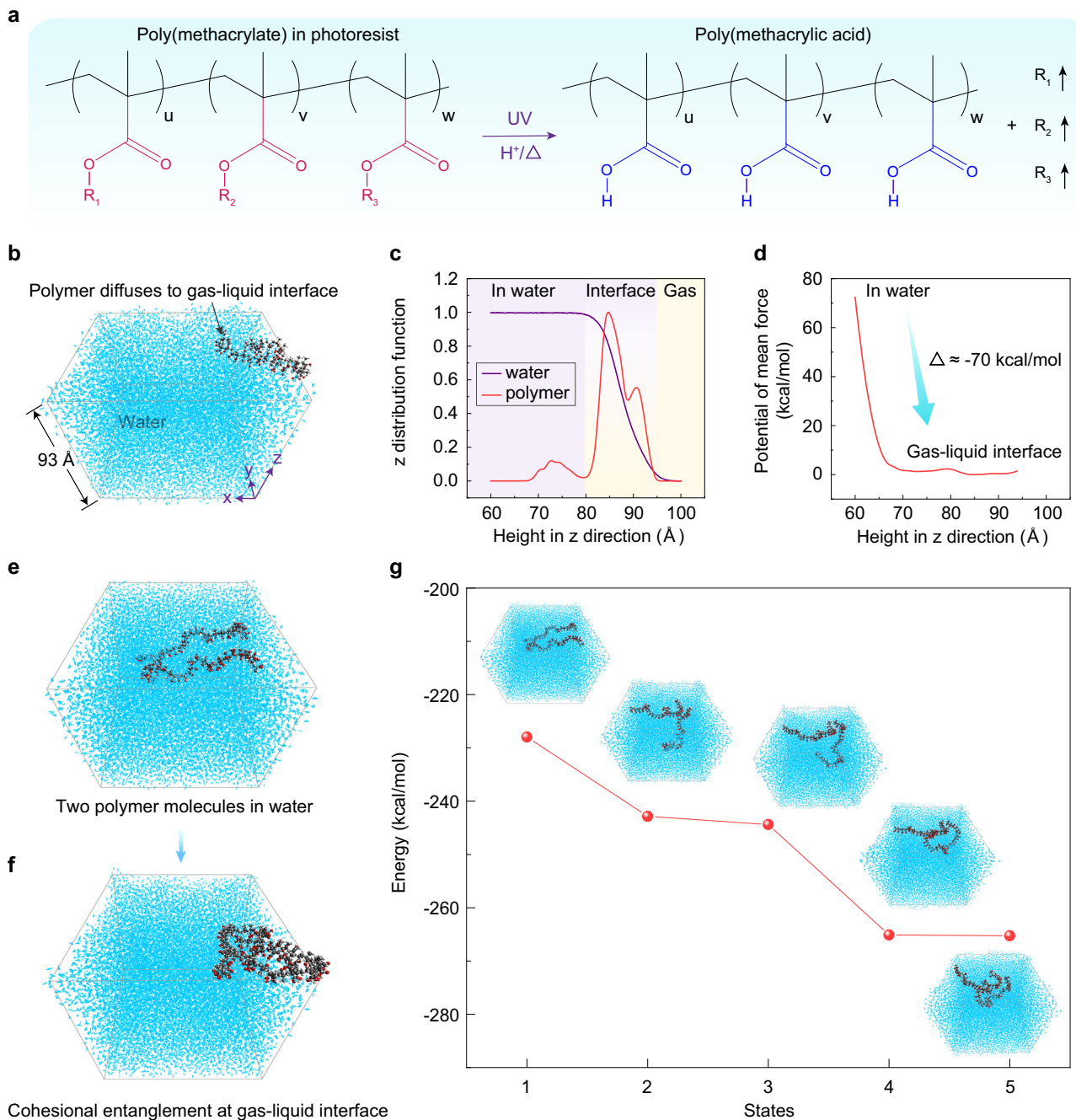


**Fig. 4 | Molecular dynamics simulations of photoresist polymers in liquid films.** **a** Typical structural changes from poly(methacrylate) to poly(methacrylic acid) in chemical amplified resist occur after ultraviolet exposure and post exposure baking. **b** Simulation showing a poly(methacrylic acid) molecule ( $u = v = w = 10$ ) diffuses to gas-liquid interface from solution interior. **c** z-distribution functions of poly(methacrylic acid) (red) and water (purple) extracted from (b). **d** Potential of mean force of poly(methacrylic acid) derived from the z-direction

distribution function in (c). **e-f** MD simulations showing two separated poly(methacrylic acid) molecules diffuse to gas-liquid interface and exhibit cohesional entanglement. **g** Energies of different states of poly(methacrylic acid) molecules. The cohesional entanglement between two poly(methacrylic acid) molecules leads to a decrease in energy. Water molecules are depicted as cyan triangles, and the C, O, and H atoms in poly(methacrylic acid) are colored black, red, and white, respectively.

temperature was increased to 105 °C (Fig. 5g, right panel). The inhibited photoresist entanglement contributes to a significant improvement in defect control (Fig. S16). Meanwhile, we recommended a continuous liquid film throughout the photoresist development process to ensure the reliable trapping of disentangled polymers at the gas-liquid interface and prevent their redeposition (Fig. 5h, S16a, S17). By leveraging such strategy, defects caused by polymer residues can be eliminated over the entire 12 inch wafer (Fig. 5i). This strategy has also demonstrated its efficiency and reliability, consistently achieving

a > 99% improvement in reducing the defects of developed patterns on the 12 inch wafers (Fig. 5j, Figs. S15, S16). Moreover, this strategy is compatible with modern fabs, where inhibited photoresist entanglements and continuous liquid films can be technically available with existing facilities.

## Discussion

For decades, the understandings of microscopic behaviors of photoresist in liquid films have been constrained by inadequate

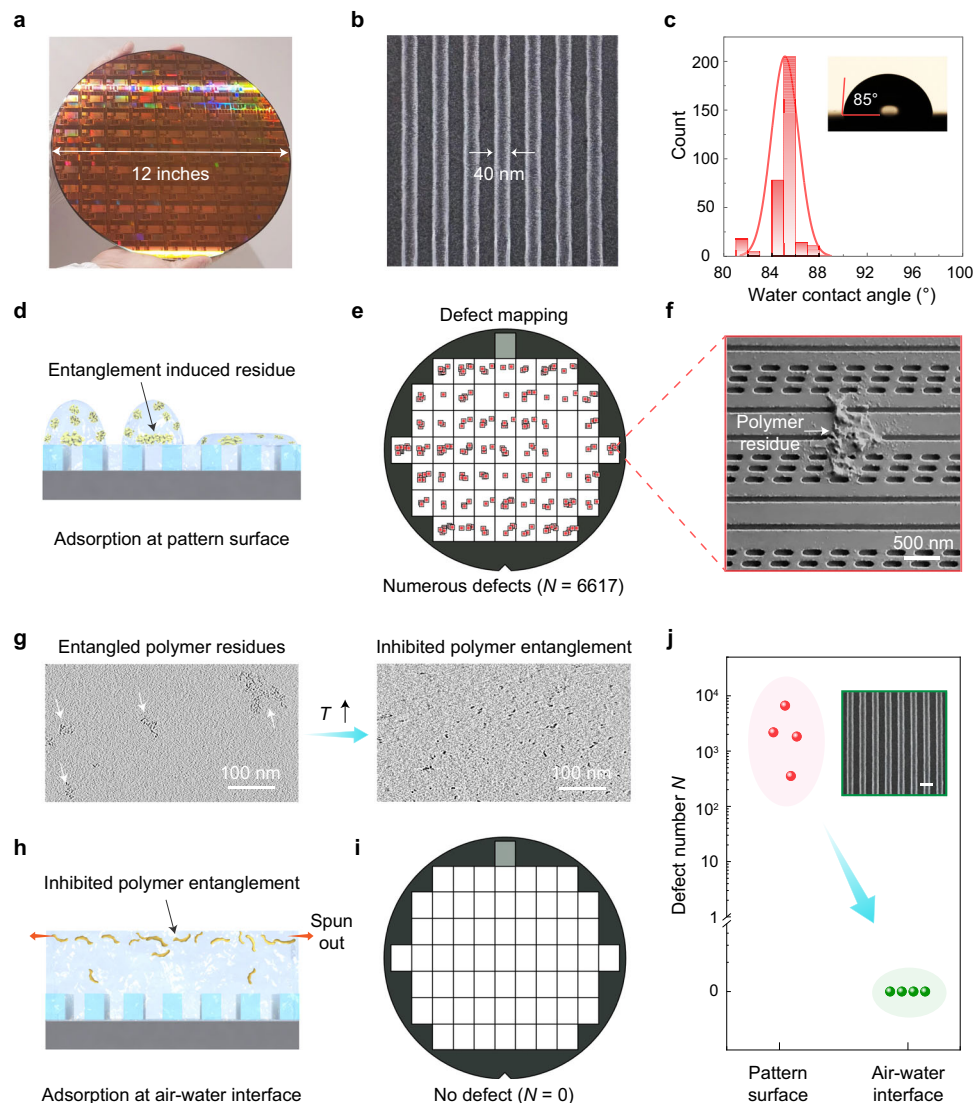


**Fig. 5 | Defect removal for fab-compatible photoresist development.** **a** Optical image of a 12 inch wafer after photoresist development. **b** SEM image of developed nanopatterns. **c** Water contact angle measurements of photoresist (chemical amplified resist). Inset: optical image showing a water contact angle of  $\sim 85^\circ$  for photoresist. **d** Schematic showing that poor wettability of photoresist leads to the adsorption of entangled polymer on the pattern surface. **e, f** Defect mapping of a 12 inch wafer after photoresist development (**e**), where each red spot indicates pattern defect occurrence (**f**). **g** cryo-ET slices showing inhibited polymer

entanglement when increasing the post exposure bake temperature ( $T$ ) from  $95^\circ\text{C}$  (left) to  $105^\circ\text{C}$  (right). **h** Schematic of defect removal by inhibiting polymer entanglement at the gas-liquid interface, preventing the formation and deposition of large-sized polymer residues. **i** A 12 inch wafer with eliminated defects. **j** A  $>99\%$  improvement has been achieved in reducing the polymer residues of developed patterns by inhibiting polymer entanglement at gas-liquid interface. Inset: typical SEM image of defect-free developed pattern. Scale bar, 80 nm.

characterization methods. This work introduces a cryo-ET imaging technique to unravel the nanostructures and dynamics of photoresist polymers in liquid films. Cryo-ET has addressed fundamental limitations in conventional approaches by enabling high-resolution 3D reconstruction of native-state structures, spatial distributions, and polymer entanglements in hydrated photoresist systems. The cryo-ET exhibits its significant advantage in reconstructing the gas-liquid interface, visualizing the preferential adsorption behavior of photoresist polymers at gas-liquid interface and resolving their cohesional entanglements at sub-5 nm resolution. These microscopic behaviors are supported by MD simulations and advance current understandings of photoresist development process. By leveraging these findings, we successfully exploited a fab-compatible strategy to remove the photoresist residues on the patterned surface across a 12 inch wafer.

Looking ahead, the reconstruction of gas-liquid interface presented in this work, paves a way for deciphering the structures and

dynamics in chemical reactions at aqueous interfaces, where the formulation of a theory remains in its early stages<sup>3,32</sup>. The cryo-ET also shows great potential for resolving the entanglements which are ubiquitous in polymer science<sup>33</sup>, additive manufacturing<sup>34</sup> and life science<sup>35</sup>. In terms of applications in semiconductor industry, the polymer nanoarchitectures and dynamics in liquid films are expected to benefit the defect control in the fields of lithography, etch and wet processes critical for fabricating next-generation electronics.

## Methods

### Lithography and photoresist development process

The commercially available methacrylate-based chemically amplified resist (AEX4459JN, positive photoresist) was spin-coated onto a rotated wafer. The rotational speed and time were 600 - 2000 rpm and 50 s, respectively. Then the photoresist film on the wafer was soft-baked at  $105^\circ\text{C}$  for 60 s to remove excess solvent. After cooling, the

lithography exposure was performed under a 193 nm laser with an energy of -34 mJ in a lithography system or an electron beam direct writing system with a voltage of 80 kV. The post exposure bake temperature and time are 90 - 105 °C and 60 s, respectively. The wafer-scale photoresist development process was performed in a track (Lithius ProZ), where the photoresist film experienced the procedures of pre-wet, pre-development, rinse, main development, rinse and spin-drying. The rotational speeds in these processes are controlled at 1000 - 2000 rpm.

### Cryo-ET specimen preparation of photoresist polymers in vitrified liquid film

A TEM grid (Quantifoil, Cu or Au, 300 mesh) was subjected to a glow discharge for 30 s under an argon gas flow of 5 sccm in a plasma cleaning system (Gatan Solarus). Then a 3  $\mu$ L TMAH developer solution containing photoresist polymers was pipetted onto the grid. The grid was subsequently transferred into a Vitrobot Mark IV (ThermoFisher Scientific) for cryo-specimen preparation. The temperature of the Vitrobot chamber was set to 8 °C with a humidity of 100%, and the blotting time was set to 1.0 - 2.5 s with a force of -2. The grid was then plunged into liquid ethane and stored in liquid nitrogen for further cryo-ET imaging. Note that the specimen thickness could be controlled by varying the blotting time.

### Cryo-ET data acquisition and processing

Cryo-ET tilt series were acquired using Titan Krios electron microscope (Thermo Fisher Scientific), equipped with a GIF Quantum post-column energy filter (Gatan) and a high-performance K3 direct detector camera (Gatan). Data were captured using SerialEM<sup>36</sup> software in dose-fractionation mode. The tilt-series was acquired through a dose-symmetric protocol<sup>37</sup>, with a finely calibrated pixel size of 1.36 Å. The imaging parameters included a defocus of -5  $\mu$ m, tilt increment of 3°, and a consistent imaging dose of 3 e/Å<sup>2</sup> across every tilt. The tilt-series spanned a range from +60° to -60°, initiated at 0°, resulting in an accumulated total dose of -123 e/Å<sup>2</sup>.

The tilt series data were imported into Warp software<sup>38</sup> for motion correction and contrast transfer function (CTF) estimation. Subsequently, the rectified tilt series were aligned within IMOD using patch-tracking<sup>39</sup>. The finely aligned series were reconstructed using a weighted back-projection method. For enhanced visualization, the 8 $\times$  binned tomograms underwent missing wedge correction via IsoNet<sup>40</sup>. These corrected tomograms were then rendered in UCSF Chimera using surface visualization mode (2.3 $\sigma$  contour level)<sup>41</sup>.

### AFM and SEM characterizations of developed pattern and defect

The structures of developed patterns were characterized by a commercial AFM tool (Bruker Dimension Icon) in contact mode with an AFM tip (SCANASYST-AIR, Bruker). The material, tip radius, resonance frequency and spring constant of this AFM tip are silicon, 650 nm, 70 kHz and 0.4 N/m, respectively. The data collection rate is 1 line/s for 256 lines.

The critical dimension and defect of developed patterns were imaged using a commercial SEM (Tescan Clara or Hitachi 6300). The operational parameters for the Tescan Clara SEM were as follows: an acceleration voltage of 5 kV, an electron beam current of 54 pA, and a magnification of 50.0 kx. For the Hitachi 6300 SEM, the parameters were: an acceleration voltage of 500 V, an electron beam current of 8 pA, and a magnification of 150.0 kx. The wafer-scale defect mapping was performed utilizing a defect review SEM (AMAT G7) with an acceleration voltage of 300 V.

### XPS measurements

For surface polymer analysis, a SiO<sub>2</sub>/Si substrate (1 × 1 cm<sup>2</sup>) was placed on the solution surface to adsorb polymers at the gas-liquid interface,

leveraging liquid surface tension for substrate flotation. For bulk solution analysis, the liquid was pipetted from the solution interior and dropped onto the SiO<sub>2</sub>/Si substrate. Then, these samples were loaded in an X-ray photoelectron spectrometer equipped with monochromatic Al X-ray (Kratos Analytical Ltd., Axis Ultra) for XPS measurements.

### GPC measurement

GPC was performed on an Agilent 1260 system equipped with an Agilent Plgel 5  $\mu$ m Mixed-C column, using HPLC-grade tetrahydrofuran (THF) as the eluent at room temperature.

### Molecular dynamics simulations

All simulations were performed using SPONGE version 1.4<sup>42</sup>. Initial polymer structures were constructed by linking the monomers using Xpunge<sup>43</sup>. GAFF<sup>44</sup> force field and TPACM4<sup>44</sup> charge model was used for the monomers isobutyric acid, methyl isobutyrate and isobutyl isobutyrate. In the modeling of the monomers, two backbone hydrogen atoms were removed. Subsequently, to maintain the neutrality of these monomers, the partial charges of the remaining atoms were recalibrated using the following formula:

$$q' = q \left( 1 - \text{sign}(q) \times \frac{|q_+| - |q_-|}{|q_+| + |q_-|} \right) \quad (1)$$

In this equation,  $q'$  represents the new charge assigned to each atom,  $q$  denotes the original charge,  $\text{sign}(q)$  indicates the sign of the original charge,  $|q_+|$  and  $|q_-|$  are the absolute values of the total positive and negative original charges, respectively. In our simulations, one poly(methacrylic acid) molecule consisted of 30 isobutyric acid monomers and one poly(methacrylate) molecule consisted of 10 isobutyric acid monomers, 10 methyl isobutyrate monomers, and 10 isobutyl isobutyrate monomers. The systems were solvated in a cubic water box using the TIP3P<sup>45</sup> model for water molecules. The box had initial dimensions of 100 Å in the x and y dimensions and 80 Å in the z dimension.

Prior to the MD simulation, energy minimization was performed using the steepest descent algorithm for 5000 steps. The system was then equilibrated in an NPT ensemble at 300 K and 1 bar for 1 ns. Long-range Coulomb interactions were handled using the Smooth Particle Mesh Ewald algorithm<sup>46</sup> during this stage. After the equilibration, the system had a length of 93 Å in the z dimension.

Following equilibration, a vacuum layer was added to achieve a total box length of 200 Å along the z-axis. Then, all atoms are lifted 5 Å in the z-direction, and reflective walls were placed at 2 Å and 100 Å to model the interfaces. The Particle Mesh Convolution–Infinite Z algorithm<sup>47</sup> was employed for the slab-like long-range electrostatic interactions.

For all simulations, the SETTLE algorithm<sup>48</sup> was used to maintain the rigidity of water molecules, and the SHAKE algorithm<sup>49</sup> was applied to all other covalent bonds involving hydrogens, allowing a time step of 2 fs for the simulations. The middle scheme of Langevin dynamics<sup>50</sup> was employed to control the temperature. A cutoff of 8 Å was set for short-range non-bonded interactions. To ensure the robustness of the simulations, three independent runs were conducted for each system, and the results were found to be reproducible.

The snapshots of the trajectories were rendered using VMD<sup>51</sup>. The analysis of ZDF was performed using custom scripts, and the ZDF data was normalized to a maximum value of 1. PMF was directly estimated from the ZDF data using the following equation:

$$\text{PMF} = k_B T \ln \text{ZDF} + C \quad (2)$$

where  $k_B$  is the Boltzmann constant,  $T = 300$  K, and  $C$  is a constant.

## Data availability

Data supporting the findings in this manuscript are available from the corresponding authors upon requests. The source data for Figs. 3b, c, 3g, 4c, d, 4g, 5c, 5j, S4c, S4f, S8c, S10, S12c-d, S14c, S14f, and S17b generated in this study are provided in the Source Data file. Source data are provided with this paper.

## References

- Hong, J. N. et al. Imaging surface structure and premelting of ice Ih with atomic resolution. *Nature* **630**, 375–380 (2024).
- Zhang, H. et al. Freezing droplet ejection by spring-like elastic pillars. *Nat. Chem. Eng.* **1**, 765–773 (2024).
- Ruiz-Lopez, M. F., Francisco, J. S., Martins-Costa, M. T. C. & Anglada, J. M. Molecular reactions at aqueous interfaces. *Nat. Rev. Chem.* **4**, 459–475 (2020).
- Li, S. M. et al. Sleep deprivation induces corneal epithelial progenitor cell over-expansion through disruption of redox homeostasis in the tear film. *Stem Cell Rep.* **17**, 1507–1508 (2022).
- Totzeck, M., Ulrich, W., Göhnermeier, A. & Kaiser, W. Semiconductor fabrication - pushing deep ultraviolet lithography to its limits. *Nat. Photonics* **1**, 629–631 (2007).
- Lin, B. J. The  $k_3$  coefficient in nonparaxial  $\lambda/NA$  scaling equations for resolution, depth of focus, and immersion lithography. *J. Microlith. Microfab. Microsyst.* **1**, 7–12 (2002).
- International Roadmap for Devices and Systems. (IRDS™) lithography & patterning. In *IEEE International Roadmap for Devices and Systems, "Lithography and Patterning."* Institute of Electrical and Electronics Engineers (IEEE, 2023).
- Wagner, C. & Harned, N. EUV LITHOGRAPHY lithography gets extreme. *Nat. Photonics* **4**, 24–26 (2010).
- Tallents, G., Wagenaars, E. & Pert, G. OPTICAL LITHOGRAPHY Lithography at EUV wavelengths. *Nat. Photonics* **4**, 809–811 (2010).
- Wang, X. L. et al. Trends in photoresist materials for extreme ultraviolet lithography: a review. *Mater. Today* **67**, 299–319 (2023).
- Li, L. et al. Extreme ultraviolet resist materials for sub-7 nm patterning. *Chem. Soc. Rev.* **46**, 4855–4866 (2017).
- Kazazis, D., Santaclara, J. G., van Schoot, J., Mochi, I. & Ekinci, Y. Extreme ultraviolet lithography. *Nat. Rev. Method Prime* **4**, 84 (2024).
- Long, L. K., Chen, J. J., Neureuther, A., Naulleau, P. & Ashby, P. Spatially-resolved dissolution monitoring using AFM. *Proc. SPIE* **12292**, 1229206 (2022).
- Itani, T. & Santillan, J. J. Characterization of photoresist dissolution. *Appl. Phys. Express* **3**, 061601 (2010).
- Sekiguchi, A., Konishi, H. & Isono, M. Observation of swelling behavior of ArF resist during development by using QCM method. *Proc. SPIE* **8325**, 83251 (2012).
- AAAS. 125 Questions: Exploration and Discovery. sjtu-booklet.pdf (2021).
- Ober, C. K., Käfer, F. & Yuan, C. Y. Recent developments in photoresists for extreme-ultraviolet lithography. *Polymer* **280**, 126020 (2023).
- Wang, Q. Q. et al. Exceptional light sensitivity by thiol-ene click lithography. *J. Am. Chem. Soc.* **145**, 3064–3074 (2023).
- Liu, T. Q. et al. Ultrahigh-printing-speed photoresists for additive manufacturing. *Nat. Nanotech.* **19**, 51–57 (2024).
- Dubochet, J. et al. Cryo-electron microscopy of vitrified specimens. *Q. Rev. Biophys.* **21**, 129–228 (1988).
- Naydenova, K., Jia, P. P. & Russo, C. J. Cryo-EM with sub-1 Å specimen movement. *Science* **370**, 223 (2020).
- Li, Y. Z. et al. Atomic structure of sensitive battery materials and Interfaces revealed by cryo-electron microscopy. *Science* **358**, 506–510 (2017).
- Yuan, X. T., Liu, B., Mecklenburg, M. & Li, Y. Z. Ultrafast deposition of faceted lithium polyhedra by outpacing SEI formation. *Nature* **620**, 86 (2023).
- Choi, H. S. et al. Molecularly thin, two-dimensional all-organic perovskites. *Science* **384**, 60–66 (2024).
- Cattani, G., Vogeley, L. & Crowley, P. B. Structure of a PEGylated protein reveals a highly porous double-helical assembly. *Nat. Chem.* **7**, 823–828 (2015).
- Shimoaoki, T., Naito, R. & Kitano, J. Mechanisms of defect generation in chemically amplified resist processes. *Proc. SPIE* **5376**, 1223–1232 (2004).
- Ono, Y., Shimoaoki, T., Naito, R. & Kitano, J. Behavior of chemically amplified resist defects in TMAH solution (3). *Proc. SPIE* **5376**, 1206–1214 (2004).
- Porter, R. ogerS. J. F. J. The entanglement concept in polymer systems. *Chem. Rev.* **66**, 1–27 (1966).
- Kong, D. C. et al. Control of polymer properties by entanglement: a review. *Macromol. Mater. Eng.* **306**, 2100536 (2021).
- Qian, R. Y. The concept of cohesive entanglement. *Macromol. Symp.* **124**, 15–26 (1997).
- Sanders, D. P. Advances in patterning materials for 193 nm immersion lithography. *Chem. Rev.* **110**, 321–360 (2010).
- Gonella, G. et al. Water at charged interfaces. *Nat. Rev. Chem.* **5**, 466–485 (2021).
- Kim, J., Zhang, G. G., Shi, M. X. & Suo, Z. G. Fracture, fatigue, and friction of polymers in which entanglements greatly outnumber cross-links. *Science* **374**, 212 (2021).
- Dhand, A. P. et al. Additive manufacturing of highly entangled polymer networks. *Science* **385**, 566–572 (2024).
- Patil, V. P. et al. Ultrafast reversible self-assembly of living tangled matter. *Science* **380**, 392 (2023).
- Mastronarde, D. N. Automated electron microscope tomography using robust prediction of specimen movements. *J. Struct. Biol.* **152**, 36–51 (2005).
- Hagen, W. J. H., Wan, W. & Briggs, J. A. G. Implementation of a cryo-electron tomography tilt-scheme optimized for high resolution subtomogram averaging. *J. Struct. Biol.* **197**, 191–198 (2017).
- Tegunov, D., Xue, L., Dienemann, C., Cramer, P. & Mahamid, J. Multi-particle cryo-EM refinement with M visualizes ribosome-antibiotic complex at 3.5 Å in cells. *Nat. Methods* **18**, 186 (2021).
- Tegunov, D. & Cramer, P. Real-time cryo-electron microscopy data preprocessing with warp. *Nat. Methods* **16**, 1146 (2019).
- Kremer, J. R., Mastronarde, D. N. & McIntosh, J. R. Computer visualization of three-dimensional image data using IMOD. *J. Struct. Biol.* **116**, 71–76 (1996).
- Pettersen, E. F. et al. UCSF chimera - a visualization system for exploratory research and analysis. *J. Comput. Chem.* **25**, 1605–1612 (2004).
- Huang, Y.-P. et al. SPONGE: A GPU-accelerated molecular dynamics package with enhanced sampling and ai-driven algorithms. *Chin. J. Chem.* **40**, 160–168 (2022).
- Xia, Y. & Gao, Y. Q. Xponge: A python package to perform pre- and post-processing of molecular simulations. *J. Open Source Softw.* **7**, 4467 (2022).
- Mukherjee, G., Patra, N., Barua, P. & Jayaram, B. A Fast empirical GAFF compatible partial atomic charge assignment scheme for modeling interactions of small molecules with biomolecular targets. *J. Comput. Chem.* **32**, 893–907 (2011).
- Shirts, M. R. & Pande, V. S. Comparison of efficiency and bias of free energies computed by exponential averaging, the Bennett acceptance ratio, and thermodynamic integration. *J. Chem. Phys.* **122**, 144107 (2005).
- Saffar Shamshirgar, D., Hess, B. & Tornberg, A.-K. A comparison of the spectral Ewald and smooth particle mesh Ewald methods in GROMACS. *arXiv* <https://doi.org/10.48550/arXiv.1712.04718> (2017).
- Huang, Y.-P., Xia, Y., Yang, L. & Gao, Y. Q. P. M. C.-I. Z. A simple algorithm for the electrostatics calculation in slab geometric

molecular dynamics simulations. *J. Chem. Theory Comput.* **20**, 832–841 (2024).

- 48. Miyamoto, S. & Kollman, P. A. Settle: An analytical version of the SHAKE and RATTLE algorithm for rigid water models. *J. Comput. Chem.* **13**, 952–962 (1992).
- 49. Ryckaert, J.-P., Ciccotti, G. & Berendsen, H. J. C. Numerical integration of the cartesian equations of motion of a system with constraints: molecular dynamics of n-alkanes. *J. Comput. Phys.* **23**, 327–341 (1977).
- 50. Zhang, Z. et al. A unified thermostat scheme for efficient configurational sampling for classical/quantum canonical ensembles via molecular dynamics. *J. Chem. Phys.* **147**, 034109 (2017).
- 51. Humphrey, W., Dalke, A. & Schulten, K. V. M. D. visual molecular dynamics. *J. Mol. Graph* **14**, 33–38 (1996).

## Acknowledgements

L.Z. thank Junchuan Tang, Chenxi Zhang, Hongfang Wang and Hongtao Liu for fruitful discussions. We acknowledge Molecular Materials and Nanofabrication Laboratory (MMNL) in the College of Chemistry at Peking University for the use of instruments. We acknowledge financial support from the National Natural Science Foundation of China (22402007 to L.M.Z.; 52021006 to H.L.P.; 31825009 to H.-W.W.; 21821004 and 22463003 to Y.Q.G.; 32200981 to N.L.), National Key Research and Development Program of China (2024YFA1307301 to H.-W.W.), Beijing National Laboratory for Molecular Sciences (BNLMS-CXTD-202001), the XPLORER PRIZE (to H.-W.W. and H.L.P.), and the New Cornerstone Science Foundation (NCI202305 to Y.Q.G.).

## Author contributions

L.Z. and H.P. conceived the project and designed the experiments. N.L., X.J., L.Z., J.S., X.L. and H.-W.W. carried out the cryo-ET characterizations and analysis. Y.X., L.Y. and Y.G. performed the MD simulations. L.Z. and M.G. contributed to the lithography and wafer-scale photoresist development. L.Z. and X.Z. performed AFM characterizations. L.Z. and X.G. characterized the SEM imaging of the developed pattern. L.Z. measured the water contact angle of photoresist film. W.Z. measured the molecular weight of photoresist. Q.W. and W.K provided the photoresist. The manuscript was written by L.Z., H.-W.W. and H.P. with input from the other authors. All authors discussed the results and commented on the manuscript. All authors have given approval to the final version of the manuscript.

## Competing interests

The authors declare no competing interests.

## Additional information

**Supplementary information** The online version contains supplementary material available at <https://doi.org/10.1038/s41467-025-63689-4>.

**Correspondence** and requests for materials should be addressed to Nan Liu, Yiqin Gao, Hong-Wei Wang or Hailin Peng.

**Peer review information** *Nature Communications* thanks Tiger Tao and the other, anonymous, reviewer for their contribution to the peer review of this work. A peer review file is available.

**Reprints and permissions information** is available at <http://www.nature.com/reprints>

**Publisher's note** Springer Nature remains neutral with regard to jurisdictional claims in published maps and institutional affiliations.

**Open Access** This article is licensed under a Creative Commons Attribution-NonCommercial-NoDerivatives 4.0 International License, which permits any non-commercial use, sharing, distribution and reproduction in any medium or format, as long as you give appropriate credit to the original author(s) and the source, provide a link to the Creative Commons licence, and indicate if you modified the licensed material. You do not have permission under this licence to share adapted material derived from this article or parts of it. The images or other third party material in this article are included in the article's Creative Commons licence, unless indicated otherwise in a credit line to the material. If material is not included in the article's Creative Commons licence and your intended use is not permitted by statutory regulation or exceeds the permitted use, you will need to obtain permission directly from the copyright holder. To view a copy of this licence, visit <http://creativecommons.org/licenses/by-nc-nd/4.0/>.

© The Author(s) 2025